Physics Letters A 382 (2018) 2886–2893

Contents lists available at ScienceDirect

Physics Letters A

www.elsevier.com/locate/pla

Annealing effect of NiO/$Co_{90}Fe_{10}$ thin films: From bilayer to nanocomposite

Xu Li [a,b], Yu-Chi Chang [c], Jiann-Yeu Chen [d], Ko-Wei Lin [c,d,*], Ryan D. Desautels [e], Johan van Lierop [f,**], Philip W.T. Pong [b,**]

[a] Fujian Provincial Key Laboratory of Semiconductors and Applications, Collaborative Innovation Center for Optoelectronic Semiconductors and Efficient Devices, Department of Physics, Xiamen University, Xiamen 361005, PR China
[b] Department of Electrical and Electronic Engineering, The University of Hong Kong, Hong Kong
[c] Department of Materials Science and Engineering, National Chung Hsing University, Taichung 402, Taiwan
[d] Research Center for Sustainable Energy and Nanotechnology, National Chung Hsing University, Taichung 402, Taiwan
[e] Quantum Condensed Matter Division, Oak Ridge National Laboratory, Oak Ridge, TN 37831, USA
[f] Department of Physics and Astronomy, University of Manitoba, Winnipeg, R3T 2N2, Canada

ARTICLE INFO

Article history:
Received 26 February 2018
Received in revised form 10 July 2018
Accepted 12 July 2018
Available online 17 July 2018
Communicated by M. Wu

Keywords:
Exchange bias
Magnetic thin film
Nanocomposite

ABSTRACT

Exchange-biased bilayers are widely used in the pinned layers of spintronic devices. While magnetic field annealing (MFA) was routinely engaged during the fabrication of these devices, the annealing effect of NiO/CoFe bilayers is not yet reported. In this paper, the transition from NiO/$Co_{90}Fe_{10}$ bilayer to nanocomposite single layer was observed through rapid thermal annealing at different temperatures under magnetic field. The as-deposited and low-temperature (<623 K) annealed samples had rock salt (NiO) and face center cubic ($Co_{90}Fe_{10}$) structures. On the other hand, annealing at 623 K and 673 K resulted in nanocomposite single layers composed of oxides (matrix) and alloys (precipitate), due to grain boundary oxidization and strong interdiffusion in the NiO/CoFe and CoFe/SiO_2 interfaces. The structural transition was accompanied by the reduction of grain sizes, re-ordering of crystallites, incensement of roughness, and reduction of Ni^{2+}. When measured at room temperature, the bilayers exhibited soft magnetism with small room-temperature coercivity. The nanocomposite layers exhibited an enhanced coercivity due to the changes in the magnetization reversal mechanism by pinning from the oxides. At 10 K, the increased antiferromagnetic anisotropy in the NiO resulted in enhanced coercivity and exchange bias in the bilayers. The nanocomposites exhibited weaker exchange bias compared with the bilayers due to frustrated interfacial spins. This investigation on how the magnetic properties of exchange-biased bilayers are influenced by magnetic RTA provides insights into controlling the magnetization reversal properties of thin films.

1. Introduction

The exchange coupling has been studied intensively [1–4] for widespread application in spintronic devices such as hard disk drive reading heads. This exchange coupled phenomenon is typically characterized by a shift in the magnetic hysteresis loop (exchange bias field, H_{ex}), and an enhanced coercivity (H_c). The exchange bias effect relies on many parameters, including magnetic domain structures [5], FM and AF anisotropies [6–8], interfacial microstructures [9], and interfacial spin configurations [10,11]. Magnetic field annealing (MFA) [12–14] is an effective method for modifying the microstructure and altering H_c and H_{ex} of exchange-coupled films [15]. In metal/NiO systems, annealing at a moderate temperature of 573 K results in oxidization of metallic atoms due to the migration of O^{2-} from the NiO layer [16]. Significant interdiffusion of Fe and Ni atoms was reported in a Fe/NiO bilayer annealed at 723 K [17]. High-temperature annealing at 873 K resulted in significant interdiffusion in FePt/TiO_x bilayers, and a nanocomposite layer of FePt grains with TiO_x boundaries was formed [18]. These investigations have revealed that the annealing temperature plays a dominant role in the effect of MFA on the film composition and magnetism. Conventional MFA was conducted in a furnace, where grain growth is frequently observed in the heating and cooling period due to the slow heating and

* Corresponding author at: Department of Materials Science and Engineering, National Chung Hsing University, Taichung 402, Taiwan.
** Corresponding authors.
E-mail addresses: kwlin@dragon.nchu.edu.tw (K.-W. Lin), johan@physics.umanitoba.ca (J. van Lierop), ppong@eee.hku.hk (P.W.T. Pong).

https://doi.org/10.1016/j.physleta.2018.07.018
0375-9601/

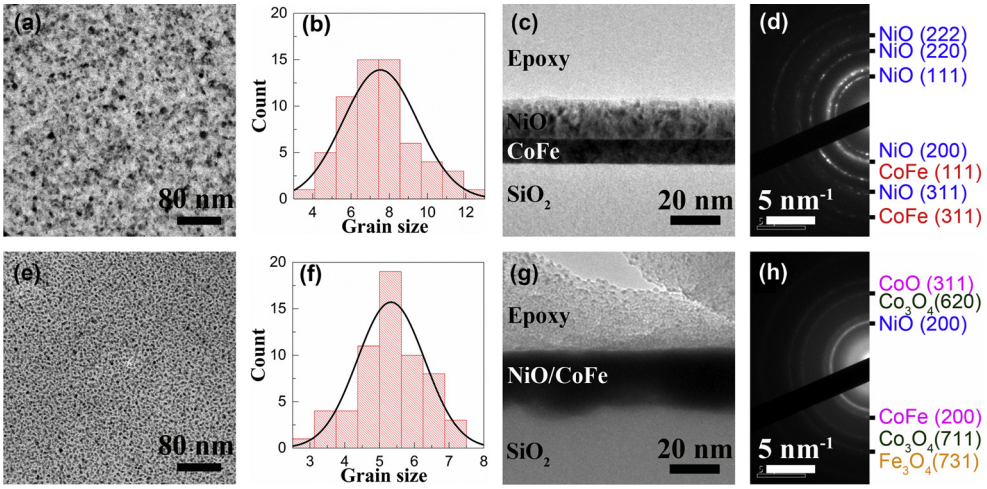

Fig. 1. TEM characterizations of NiO/CoFe thin films: (a), (b), (c), (d) and (e), (f), (g), (h) represent the planar view, grain-size distribution, cross-sectional view, and electron diffraction patterns of the as-deposited and annealed (673 K [down]) samples, respectively.

cooling rates. The rapid thermal annealing (RTA) technique engages much faster heating rate and shorter annealing time, thus offering flexibility in controlling the crystallization and phases. RTA was reported to greatly reduce the required temperature for phase transition [19]. This technique was frequently used to fabricate nanocomposite thin films [20,21], which hold promise for storage applications [22].

NiO is a commonly used AF material in the pinned layers of spin valves. The previous works have revealed the influence of the composition of NiO [23,24], post-deposition ion-beam bombardment [8], single crystalline substrate [15], and interfacial roughness [25] on the exchange bias of FM/NiO bilayers. The changes in the deposition [26] and annealing temperature [27] altered the microstructure of NiO layer and modified the exchange coupling with the subsequently deposited NiFe layer. However, the effect of post-deposition annealing on NiO/CoFe bilayer has not yet been reported. In this work, magnetic RTA was engaged to modify the microstructure and magnetic properties of CoFe/NiO bilayers. This study is beneficial for understanding the annealing effect of spintronic devices that engage CoFe/NiO pinned layers.

2. Experimental details

The NiO (15 nm)/CoFe (10 nm) bilayers were prepared by dual ion-beam sputtering deposition technique [28,29] on thermally oxidized Si substrates. A Kaufman ion source (800 V, 7.5 mA) was used to focus the argon ion beam onto a commercial $Co_{90}Fe_{10}$ (at%) target to deposit the bottom layer. The End-Hall ion source (V_{EH} = 70 V, 500 mA) was used to oxidize the Ni atoms into NiO during Ni deposition with a fixed 16% oxygen and argon gases ratio. No magnetic field was applied during deposition. The base and working pressures were 4×10^{-5} Pa and 6.7×10^{-2} Pa, respectively.

The as-deposited thin films were annealed in vacuum (0.13 Pa) under 0.3 T in-plane magnetic field. The heating was performed by a tungsten filament with a temperature gradient of 8.33 K/s. The heater temperature and the thin film orientation are (373 K [up]), (623 K [up]), (623 K [down]), and (673 K [down]), respectively (down indicates the thin film is facing the heater, thus having higher temperature, while up means otherwise). Relatively long annealing time (1 hour) was engaged to ensure the system reached stable state. After annealing, the samples were cooled to room temperature at 0.25 K/s.

The depth-profile of X-ray photoelectron spectra (XPS) were measured with a ULVAC-PHI PHI 5000 VersaProbe after Ar ion beam (2×2 mm^2) etching at 2 kV and 20 mA. Transmission electron microscope (TEM) images (in-plane and cross-sectional) and electron diffraction patterns were collected using a JEOL-2010 operating at 200 kV. Grazing incidence X-ray diffraction patterns were characterized by Brüker AXS D8 Advance (incident angle of 0.5 degrees). The topography and roughness were measured by Bruker Dimension Icon atomic force microscopy (AFM). The image scan size and resolution are 1×1 μm^2 and 256×256 pixels respectively. To prevent samples and the AFM tip from damage, tapping mode was carried out and the scan rate was 0.5 Hz. The AFM tip was adopted from AppNano ACSTA series with spring constant and the resonance frequency of 7.8 N/m and 150 KHz respectively. Magnetic hysteresis loops at 298 K were measured at 0°, 90°, and 180° to the annealing field by a commercial DMS vibrating sample magnetometer. The hysteresis loops at 10 K were characterized by a superconducting quantum interference device (SQUID) magnetometer. A 500 mT magnetic field was applied along the easy axes to reduce the thermal fluctuation of crystallite local spins during magnetization freezing.

3. Results and discussions

The microstructures of as-deposited and annealed (673 K [down]) samples were characterized by TEM (Fig. 1). The as-deposited bilayer exhibited polycrystalline structures with a mean grain size of 7.53 ± 0.48 nm (Fig. 1(a), (b)). A well-defined interface was observed between the NiO (top) and CoFe (bottom) layers (Fig. 1(c)). The NiO layer exhibited a rock-salt structure (a ~4.26 Å) while the CoFe layer has a face-centered cubic (a ~3.51 Å) lattice, as shown in the electron diffraction patterns (Fig. 1(d)). After annealing at 673 K with the sample facing the heater (673 K [down]), nanocrystallites with a smaller grain size of 5.33 ± 0.24 nm were observed (Fig. 1(e), (f)). The small grain size is typical for rapid thermal-annealed thin films [30]. The interface is no longer distinguishable, forming a nanocomposite single layer as shown in Fig. 1(g). The blurred bottom interface indicates strong interdiffusion with the SiO_2 substrate. The nanocomposite is composed of NiO, CoO, CoFe, Co_3O_4 and Fe_3O_4, as shown in Fig. 1(h). The formation of grains of various oxides indicates that significant intermixing and reactions occurred during the high-temperature annealing [15].

The TEM comparison revealed that the transition from a NiO/CoFe bilayer to a nanocomposite single layer was accompanied by the modified crystalline structures. XRD characterization was further performed to verify the crystalline structure changes

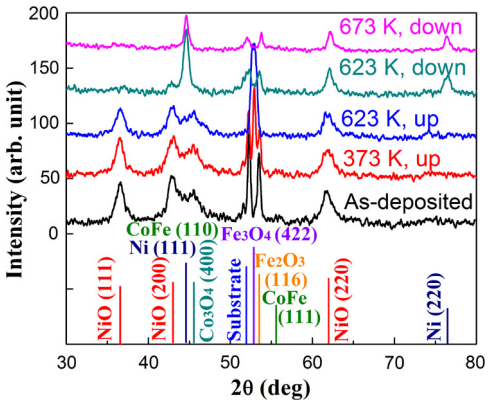

Fig. 2. XRD patterns of the as-deposited and annealed samples. (For interpretation of the colors in the figure(s), the reader is referred to the web version of this article.)

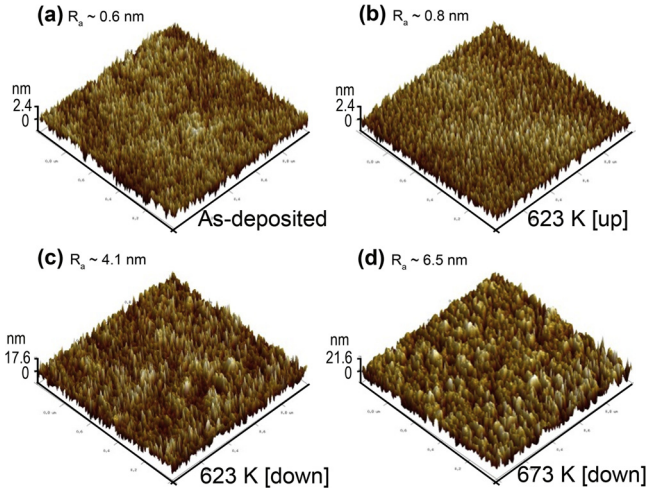

Fig. 3. 1 × 1 μm AFM images for (a) as-deposited bilayer, (b) bilayer (623 K [up]), (c) nanocomposite (623 K [down]), (d) nanocomposite (673 K [down]).

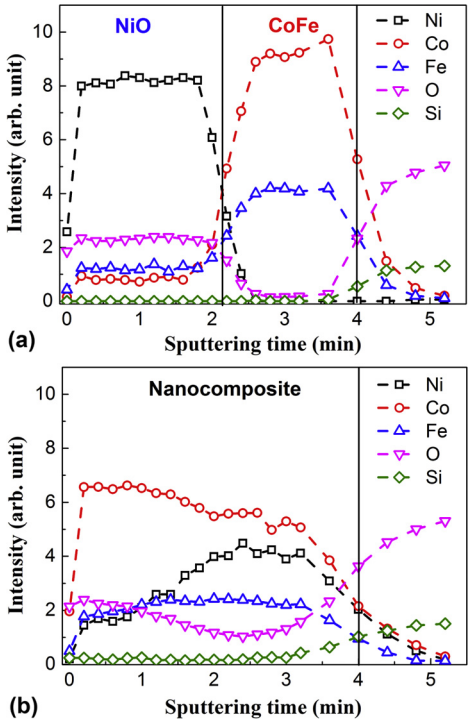

Fig. 4. Depth profile of the XPS intensity in the (a) as-deposited bilayer and (b) nanocomposite (673 K [down]).

after annealing at different temperatures. The XRD patterns in Fig. 2 can be divided roughly into two groups, corresponding respectively to the NiO/CoFe bilayer in the as-deposited and low-temperature-annealed ((373 K [up]) and (623 K [up])) samples, and the nanocomposite in high-temperature-annealed ((623 K [down]) and (673 K [down])) samples. In the as-deposited sample, intense reflection peaks from the top NiO and bottom CoFe layers were shown. Peaks from Co-oxide (Co_3O_4 (400)) and Fe-oxides (α-Fe_2O_3 (116)) were also observed. The formation of Co-oxide and Fe-oxide at interfaces are likely due to the interaction between the oxygen ions from the End-Hall source and the CoFe bottom layer during the growth of NiO top layer. In the bilayer films (373 K [up] and 623 K [up]), a new reflection peak of Fe_3O_4 (422) was visible. The XRD patterns of nanocomposite (623 K [down]) showed considerable changes compared with the bilayers. The decreased peak intensities of NiO, CoFe, Fe_2O_3, Fe_3O_4 and Co_3O_4 crystallites are attributed to the oxidization of metallic phases and reordering of preferred orientations of crystallites during annealing [31, 32]. The emergence of Ni (111) and Ni (220) peaks corresponds to the formation of metallic Ni phases. The diffraction peak at 44.6° may also be originated from the CoFe (110) phase, as the magnetic field promotes the formation of low angle grain boundaries in CoFe during annealing [33]. However, the annealing field was not strong enough to induce phase separation or reorientation inside the grains (typically several Tesla [34]). The enhanced diffusion in nanocomposite (673 K [down]) disordered the crystalline structures, which was responsible for the reduced diffraction peak intensities. Our results show unequivocally that magnetic RTA alters directly the structure and composition of NiO/CoFe thin films by promoting intermixing, creating oxides, and reordering the preferred crystalline orientations.

The influence of the annealing temperature on the microstructure was investigated with AFM. The 3D profile and average roughness (R_a) are shown in Fig. 3. The bilayers (Fig. 3(a) and (b)) exhibit a low surface roughness of less than 1 nm. The increased diffusion between the NiO and CoFe layers at high temperature [35] created more defects in the nanocomposites (623 K [down] and 673 K [down]). This mechanism is responsible for the increased roughness in Fig. 3(c) and (d). From the XRD and AFM characterization, we conclude that the transformation from bilayer to nanocomposite occurred after annealing at temperatures higher than (623 K [down]).

The structural transformation from bilayer to nanocomposite was also accompanied by the changes in chemical composition, as observed by depth-dependent XPS. The XPS depth profile of the as-deposited bilayer and nanocomposite (673 K [down]) was carried out with the Ar ion sputtering at ~7.1 nm/min (Fig. 4). In Fig. 4(a), after the sputtering time (t_{sp}) of 0.2 min, the increased content of O, Co, Fe, and Ni indicated Ar ion sputtered into the specimen. When $t_{sp} < 2.2$ min, the content of Ni and O is higher than that of Fe, Co, and Si, which confirms the formation of the NiO as the top layer of the as-deposited sample. After t_{sp} of 2.2 min, the sharp increase of the signal of Co and Fe corresponds to the CoFe layer. However, in the nanocomposite (673 K [down]), only small variation in the elemental signal was observed as the ion beam etched through the film (Fig. 4(b)). The similar atomic concentration when $t_{sp} < 3$ min indicated strong interdiffusion during the high-temperature annealing. After 3.6 min, the gradual decrease of Co, Fe and Ni Fig. 4(b) intensity indicated strong intermixing with the SiO_2 substrate after high-temperature annealing. The XPS depth-profile results confirmed the observation from the cross-sectional TEM image (Fig. 1(g)) that a single nanocomposite layer was formed.

The XPS of Ni, O, Co and Fe in the as-deposited and annealed (673 K [down]) sample are shown in Fig. 5 to further reveal the

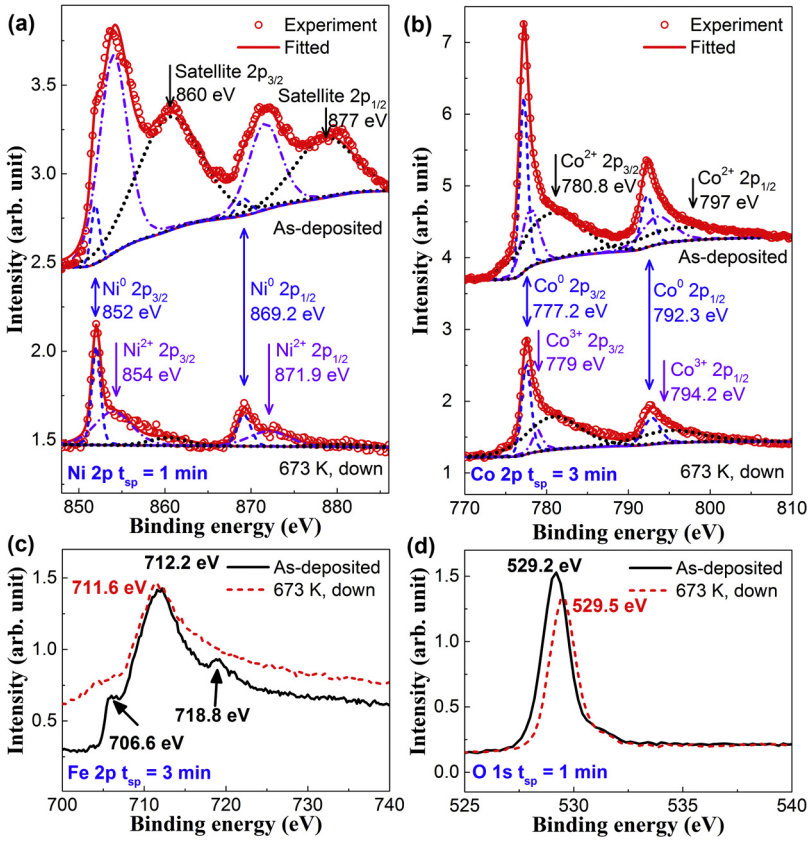

Fig. 5. The binding energies of (a) Ni 2p at $t_{sp} = 1$ min, (b) Co 2p at $t_{sp} = 3$ min, (c) Fe 2p at $t_{sp} = 3$ min, and (d) O 1s at $t_{sp} = 1$ min in the as-deposited bilayer and nanocomposite (673 K [down]).

oxidization states of metallic atoms in the bilayers and nanocomposites. In the as-deposited bilayer (Fig. 5(a)), the major peaks of Ni 2p spectra at 854 eV and 871.9 eV indicate the formation of NiO. The satellite peaks at 860 eV and 877 eV are possibly due to the emissions of Ni^{3+} ions which were formed as a result of vacancies and defects [36]. The minor Ni^0 subpeaks at 852 eV and 869.2 eV [37,38] indicated that a small portion of Ni atoms were not oxidized. On the other hand, the Ni 2p spectrum in the annealed nanocomposite film (673 K [down]) can be decomposed into the major peak of metallic Ni^0, the sub-peak of Ni^{2+}, and the weak satellite peak from defects. The dominating metallic Ni^0 signal indicated that a substantial portion of Ni^{2+} was reduced to Ni^0 due to loss of oxygen. The smaller Ni^{2+} signal is also consistent with the reduced XRD peak strength of NiO (200) (110) and (220) in the nanocomposite (Fig. 2). In the Co 2p spectrum of the as-deposited CoFe layer (Fig. 5(b)), the major peaks at 777.2 eV and 792.3 eV were resulted from the metallic Co [39]. The subpeaks at 779 eV and 794.2 eV corresponded to the Co^{3+} in naturally oxidized Co_3O_4 [40], which was also observed in the XRD results. The subpeaks at higher binding energy of 780.8 eV and 797 eV, on the other hand, were attributed to the formation of CoO [40]. In the annealed nanocomposite (673 K [down]), the weakened Co^{3+} subpeak and the strengthened Co^{2+} peak indicated that part of the Co_3O_4 and metallic Co are transformed into CoO. In Fig. 5(c), the binding energies of 706.6 eV and 712.2 eV for Fe2p 3/2 in the as-deposited bilayer indicated the formation of Fe^{2+} and Fe^{3+}, respectively [41]. The satellite peak at 718.8 eV of Fe2p 3/2 was attributed to the shake-up process [42,43] in Fe^{3+} due to the movement of electrons from the 3d to the 4s orbitals. In the nanocomposite film (673 K [down]), the reduced shoulder at 706.6 eV indicated the Fe^{2+} were oxidized into Fe^{3+} after annealing. The disappearance of the satellite peak was attributed to the higher defect density in the Fe_2O_3 nanocrystallites, which increased the conductivity and quenched the shake-up process [44]. The O 1s peak shifted towards higher energy (Fig. 5(d)) in the nanocomposite (673 K [down]) due to the higher binding energy of oxygen in CoO [45] and Fe_3O_4 [46] than NiO [47].

From the above structural and compositional characterization, we conclude that the samples change from bilayers (as-deposited, (373 K [up]) and (623 K [up])) to nanocomposites ((623 K [down]) and (673 K [down])) at higher annealing temperature. The corresponding changes in chemical composition is discussed in a thermal dynamics point of view. The enthalpy of formation for NiO and SiO_2 are −240.28 kJ/mol [48] and −850.8 kJ/mol [49], respectively. As a comparison, the enthalpy of formation for CoO, Co_3O_4, FeO, Fe_2O_3, and Fe_3O_4 are −237.9 kJ/mol [50], −891 kJ/mol [50], −270.3 kJ/mol [51], −830.5 kJ/mol [51] and −1116.7 kJ/mol [49], respectively. The high annealing temperature and the large temperature gradient in RTA promoted the interdiffusion at the NiO/CoFe and CoFe/SiO_2 interfaces, as inferred from the cross-sectional TEM and XPS. In the as-deposited bilayer, a small amount of Co and Fe atoms near the interface were oxidized into Co_3O_4, FeO, Fe_2O_3, and Fe_3O_4 due to the more negative enthalpy of formation compared with NiO and SiO_2. The nanocomposite layer was formed as a result of the grain-boundary oxidization [4,52] during annealing. At high temperatures, the oxygen ions diffused into the CoFe layer through grain boundaries, forming the oxide matrix. Meanwhile, the metallic atoms also diffused into the oxide layer. The atomic migration and grain-boundary oxidization resulted in the reduced CoFe grain size, which is consistent with the smaller crystallite size in Fig. 1(f) compared with Fig. 1(b). Some Co_3O_4 changed to CoO due to reaction with the excess Co atoms under high temperature. Meanwhile, Ni^{2+} ions in the NiO layer were reduced back to Ni^0 by the metallic Co and Fe [16], as evidenced by the enhanced Ni^0

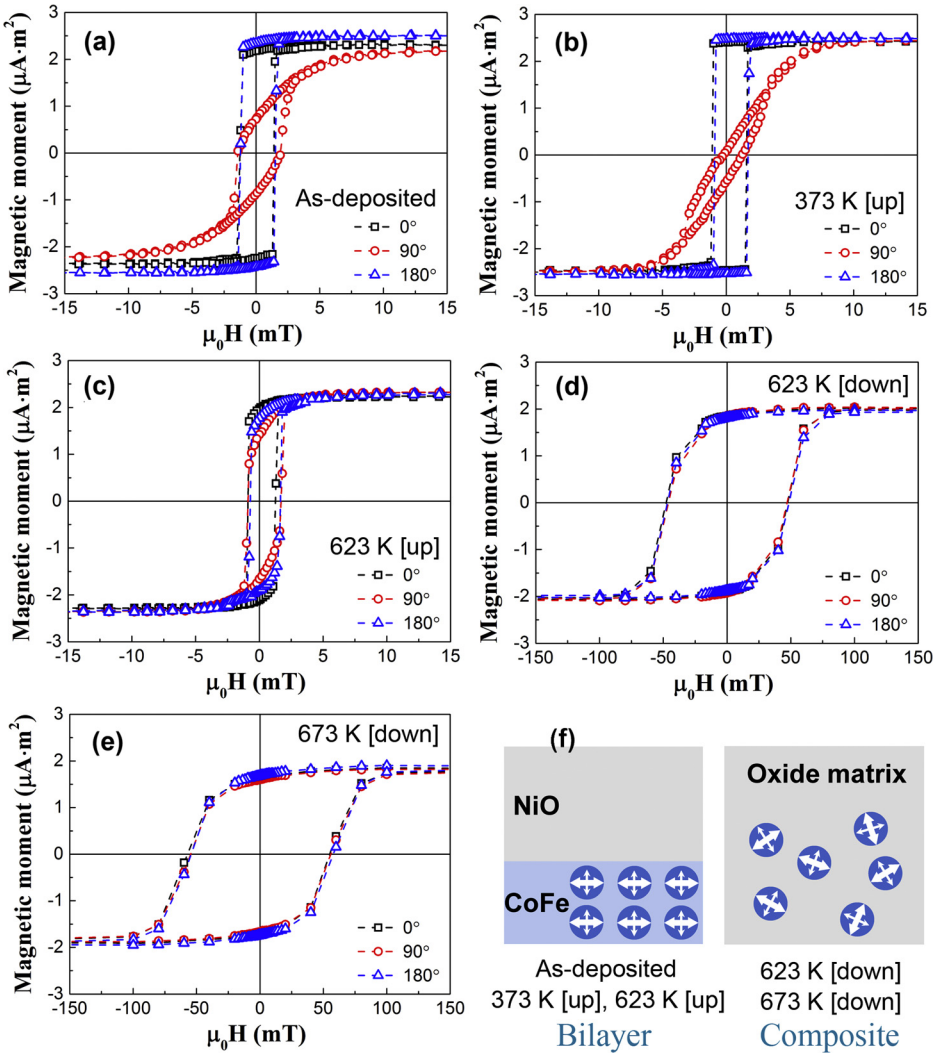

Fig. 6. The room-temperature magnetic hysteresis loops measured at 0°, 90°, and 180° to the annealing field for (a) as-deposited bilayer, (b) bilayer (373 K [up]), (c) bilayer (623 K [up]), (d) nanocomposite (623 K [down]), (e) nanocomposite (673 K [down]); and (f) the schematic of the ordering of the anisotropies in crystallites.

peak in Fig. 5(b). The metallic Ni, Co, and Fe atoms formed the alloy crystallites and they were dispersed in the oxide matrix. The changes in the microstructure and chemical composition modified the magnetic properties, as characterized below.

The in-plane magnetic hysteresis loops at 298 K and 10 K are shown in Fig. 6 and Fig. 7, respectively. At 298 K, the remanence (Mr/Ms) of the as-deposited bilayer (Fig. 6(a)) is about 0.95. However, when the measuring field direction was rotated from 0 to 90 degree in-plane, the remanence was reduced to 0.3. This isotropic behavior is mainly contributed by the magnetocrystalline anisotropy of CoFe (111) phases. The FCC CoFe exhibits a cubic magnetocrystalline anisotropy with three easy axes of [110], [1$\bar{1}$0], [110] and [001] [53,54]. The as-grown CoFe thin film is mainly composed of CoFe (110) and (111) phase, as inferred from the XRD characterization. The CoFe (110) grains exhibit a two-fold in-plane anisotropy with easy axes of [1$\bar{1}$0] and [001]. While the CoFe (111) grains have an in-plane [1$\bar{1}$0] axis and a [001] axis tiled out of plane by 57.3°. This asymmetry results in a more easy axis at CoFe (111) [1$\bar{1}$0] and a less easy axis at CoFe (111) [001]. This bi-axial behavior is also accord with the similar coercivity but distinct remanence in the "anisotropic" magnetic hysteresis loops at 0° and 90°. The low-temperature annealed bilayer (373 K [up], Fig. 6(b)) exhibited even smaller remanence at 90°. With increasing annealing temperature, this anisotropic behavior gradually diminished in the bilayers (623 K [up], Fig. 6(c)), and isotropic remanence of about 0.9 were observed in the nanocomposites (623 K [down], Fig. 6(d)) and (673 K [down], Fig. 6(e)). The different field angle dependence is attributed to the varied magnetic anisotropy distribution in the bilayer and nanocomposite films, as schematically shown in Fig. 6(f). In the bilayers, the magnetic field annealing induced a strong field-induced anisotropy in CoFe layer. In the nanocomposites, the short-range exchange interactions among the FM crystallites were weakened by the oxide matrix. As a result, the spins in the FM crystallites were not aligned by the magnetic RTA. In addition, since the grain sizes of the nanocomposite is relatively small (5.3 nm for 673 K [down]-annealed samples), the local easy axes of nanocrystallines exhibit rapid thermal fluctuation behavior [55]. The randomly orientated and rapidly fluctuating spins in the nanocrystallines resulted in the isotropic hysteresis loops. The magnetic moment measured by VSM can be used to characterize the changes of magnetization of the thin films since all the samples have the same lateral size (1 cm × 1 cm) and thickness. The decrease of saturation magnetic moment (from 2.30 ± 0.02 × 10^{-6} Am^2 in as-deposited bilayer (Fig. 6(a)) to 1.98 ± 0.02 × 10^{-6} Am^2 and 1.85 ± 0.02 × 10^{-6} Am^2 in nanocomposite (623 K [down], Fig. 6(d)) and (673 K [down], Fig. 6(e)), respectively) after annealing is attributed to the enhanced oxidization in high-temperature annealing. These results indicated that the field angle dependence and the saturation magnetization were modified by magnetic RTA. After field cooling to 10 K, the bilay-

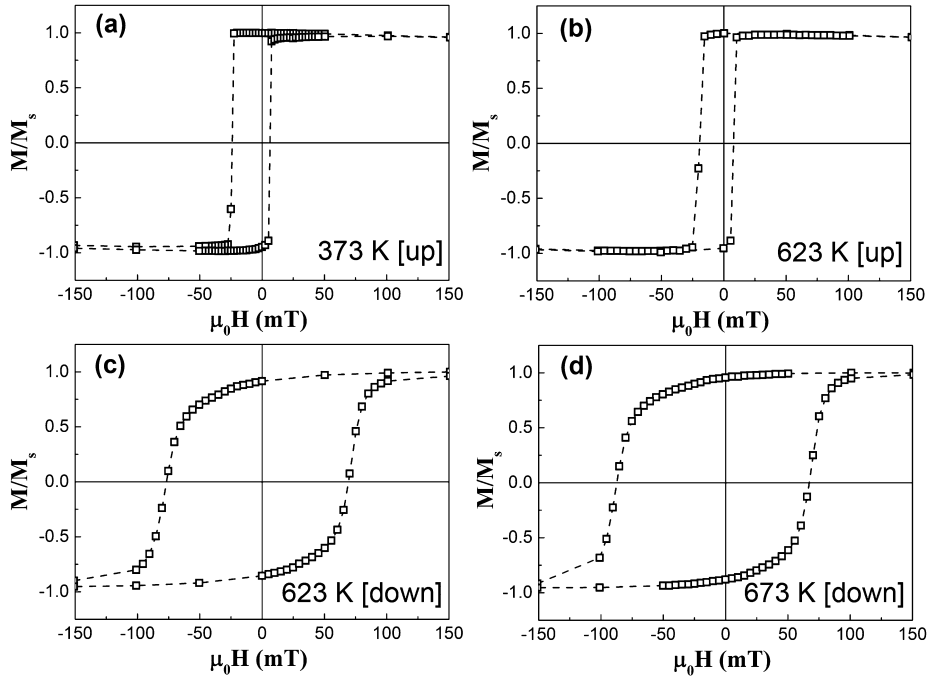

Fig. 7. The easy-axis magnetic hysteresis loops at 10 K of NiO/CoFe thin films for (a) bilayer (373 K [up]), (b) bilayers (623 K [up]), (c) nanocomposite (623 K [down]), and (d) nanocomposite (673 K [down]).

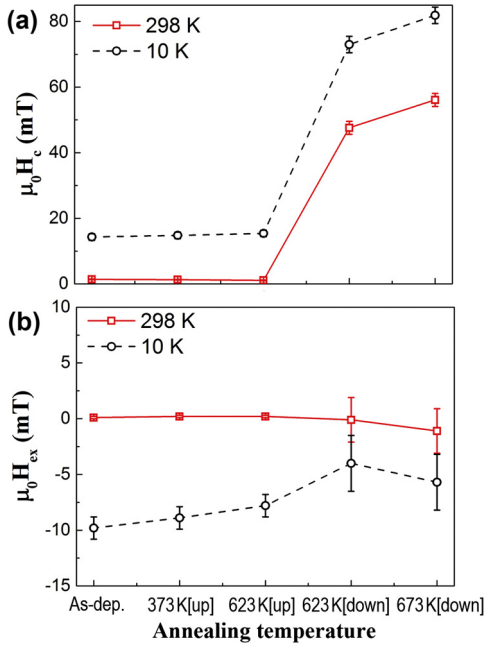

Fig. 8. (a) Easy-axes H_c and (b) H_{ex} as a function of annealing temperature at 298 K and 10 K.

ers (373 K [up], Fig. 7(a)) and (623 K [up], Fig. 7(b)) exhibited isotropic square magnetic hysteresis loop with high remanence ($M_r/M_s \sim 1$). This character indicates strongly enhanced magnetic anisotropy contributed by the magnetocrystalline anisotropy of CoFe and the exchange anisotropy between CoFe and NiO. Both the annealed bilayers and nanocomposites (623 K [down], Fig. 7(c)) and (673 K [down], Fig. 7(s)) showed broadened and shifted hysteresis loops. These changes indicated that the thermal fluctuation was suppressed at low temperature and the AF oxides established exchange coupling with the FM particles.

The easy-axis H_c and H_{ex} of all the samples are calculated and shown in Fig. 8. At 298 K, the small H_c of the as-deposited bilayer was provided by the FM CoFe layer. While H_c was nearly unchanged after annealing at relatively low temperatures ((373 K [up]) and (623 K [up])), the high-temperature annealing process resulted in loop broadening ($\mu_0 H_c = 48 \pm 2$ mT for nanocomposite (623 K [down]) and $\mu_0 H_c = 56 \pm 2$ mT for nanocomposite (673 K [down]), Fig. 8(a)). The increase in H_c was likely contributed by two factors. Firstly, the structural transition from bilayer to nanocomposite resulted in changes in magnetization reversal mechanism from domain wall motion to magnetization rotation [56] in CoFe particles, which indeed increased H_c. Secondly, the texture change into nananocrystallites and the formation of oxides (including Co_2O_3, CoO, Fe_2O_3 and Fe_3O_4) provided pinning sites to CoFe domains during magnetization reversal process. The small loop shifts (<0.2 mT) at 298 K in the bilayers indicated that interfacial exchange coupling was not yet established. This can be explained by the reduced irreversibility temperature (T_{irr}) to below 298 K since the NiO anisotropy was lowered due to finite thickness effect and disordered NiO domains [57]. A similar Tx_{irr} reduction was observed in our previously reported ion-beam bombarded thin films [58]. In the nanocomposite films, the formed oxides (K(CoO)$\sim 5\times10^5$ erg/cm^3 [59] and K(Fe_2O_3)$\sim 1.3\times10^5$ erg/cm^3 [60]) showed higher magnetocrystalline anisotropy than NiO ($\sim 3.3\times10^2$ erg/cm^3) [61]. The magnetic proximity effect between NiO (with high Néel temperature of 524 K and low anisotropy) and CoO (with low Néel temperature of 292 K and high anisotropy) yielded an antiferromagnetic oxide matrix with higher Néel temperature than CoO and higher anisotropy than NiO. Similar effect was also observed in Co/CoO core-shell particle embedded in NiO matrix [62]. The establishment of exchange interactions between the oxides and the FM particles resulted in the higher room-temperature H_{ex} in nanocomposite (623 K [down]) and (673 K [down]). The H_c and H_{ex} at 10 K were enhanced because of the AF anisotropy as exchange coupling set in [63,64]. The gradual decrease in H_{ex} with increasing annealing temperature in the bilayers (373 K [up]) and (623 K [up]) (Fig. 8(b)) was attributed to the growth of AF grains since H_{ex} is inversely proportional to AF grain size [65]. As the system was transformed into nanocomposite, decrease in H_{ex} and

increase in H_c were observed. The nanocomposite films, unlike bilayer system [5], exhibited disordered AF phases which lead to an increasing number of frustrated interfacial spins that altered the spin interactions and reduced interfacial exchange bias field [66]. The increased H_c in the nanocomposite, on the other hand, was consistent with the annealing temperature dependence at 298 K. These characterizations revealed tailored H_c and H_{ex} after annealing at different temperatures.

4. Conclusions

We investigated the microstructures and magnetic properties of NiO/CoFe thin films after RTA under magnetic field. Rock-salt NiO and face-center-cubic CoFe were formed in the as-deposited and low-temperature-annealed ((373 K [up]) and (623 K [up])) bilayers. Annealing at high temperature ((623 K [down]) and (673 K [down])) resulted in morphological changes to nanocomposite single layers composed of the metallic precipitates (Ni, Fe and Co) and oxide matrix (CoO, NiO, Co_3O_4, FeO and Fe_3O_4). These structural and compositional changes resulted in reordered crystallite orientation, increased surface roughness, modified chemical composition and tailored magnetic properties. At 298 K, the bilayers (as-deposited, (373 K [up]), and (623 K [up])) exhibited anisotropic magnetic hysteresis loops with small $\mu_0 H_c$ (2.0 ± 0.1 mT). High-temperature ((623 K [down]) and (673 K [down])) annealing resulted in isotropic loops with reduced saturation magnetization and enhanced coercivity ($\mu_0 H_c = 48 \pm 2$ mT and 56 ± 2 mT, respectively), due to the pinning effect of the oxides and the altered reversal mechanism. After field cooling to 10 K, enhanced H_c and H_{ex} were measured in all the samples, indicating the onset of exchange coupling. The relatively smaller H_{ex} in the nanocomposite films compared with the bilayer films was attributed to the frustrated interfacial spins. This work has shown that the microstructures and magnetic properties in exchange-coupled thin films could be effectively controlled through magnetic RTA at different temperatures. This technique can potentially fabricate nanocomposite thin films with large H_c and isotropic behavior for magnetic storage and novel spintronic devices.

Acknowledgements

This work was supported by the MOST of Taiwan, NSERC and CFI of Canada, Seed Funding Program for Basic Research, Seed Funding Program for Applied Research and Small Project Funding Program from the University of Hong Kong, ITF Tier 3 funding (ITS-104/13, ITS-214/14), University Grants Committee of Hong Kong (AoE/P-04/08) and Research Grants Council of Hong Kong (17204617), National Natural Science Foundation of China (No. 61674124) and Natural Science Foundation of Fujian Province of China (No. 2016J01037).

References

[1] E.Y. Chen, A.V. Pohm, J.M. Daughton, J. Brown, W.C. Black, IEEE Trans. Magn. 30 (1994) 3816–3818.
[2] A.E. Berkowitz, K. Takano, J. Magn. Magn. Mater. 200 (1999) 552.
[3] D. Lederman, J. Nogués, I.K. Schuller, Phys. Rev. B 56 (1997) 2332–2335.
[4] E. Menéndez, J. Demeter, J. Van Eyken, P. Nawrocki, E. Jedryka, M. Wójcik, J.F. Lopez-Barbera, J. Nogués, A. Vantomme, K. Temst, ACS Appl. Mater. Interfaces 5 (2013) 4320–4327.
[5] A. Brambilla, P. Sessi, M. Cantoni, M. Finazzi, N. Rougemaille, R. Belkhou, P. Vavassori, L. Duò, F. Ciccacci, Phys. Rev. B 79 (2009) 172401.
[6] J. Nogués, J. Sort, V. Langlais, V. Skumryev, S. Suriñach, J.S. Muñoz, M.D. Baró, Phys. Rep. 422 (2005) 65–117.
[7] K.-W. Lin, C. Shueh, C.-H. Liu, E. Skoropata, T.-H. Wu, J. van Lierop, J. Appl. Phys. 113 (2013) 17C104.
[8] G. Li, C.W. Leung, C. Shueh, H.-F. Hsu, H.-R. Huang, K.-W. Lin, P.T. Lai, P.W.T. Pong, Surf. Coat. Technol. 228 (2013) S437–S441.
[9] M. Perzanowski, M. Marszalek, A. Zarzycki, M. Krupinski, A. Dziedzic, Y. Zabila, ACS Appl. Mater. Interfaces 8 (2016) 28159–28165.
[10] A.P. Malozemoff, Phys. Rev. B 35 (1987) 3679–3682.
[11] D.L. Cortie, K.W. Lin, C. Shueh, H.F. Hsu, X.L. Wang, M. James, H. Fritzsche, S. Brück, F. Klose, Phys. Rev. B 86 (2012) 054408.
[12] M. Xu, Z. Lu, T. Yang, C. Liu, S. Cui, Z. Mai, W. Lai, Q. Jia, W. Zheng, J. Appl. Phys. 92 (2002) 2052–2057.
[13] A.V. Svalov, P.A. Savin, V.N. Lepalovskij, A. Larrañaga, V.O. Vas'kovskiy, A.G. Arribas, G.V. Kurlyandskaya, AIP Adv. 3 (2013) 092104.
[14] J.-Y. Guo, Y.-M. Tzeng, J.v. Lierop, S.-Y. Chang, K.-W. Lin, Jpn. J. Appl. Phys. 48 (2009) 073003.
[15] D.L. Cortie, C. Shueh, B.C. Lai, P.W.T. Pong, J. van Lierop, F. Klose, K.W. Lin, IEEE Trans. Magn. 50 (2014) 1–4.
[16] R. de Masi, D. Reinicke, F. Müller, P. Steiner, S. Hüfner, Surf. Sci. 515 (2002) 523–537.
[17] M. Finazzi, A. Brambilla, L. Duò, G. Ghiringhelli, M. Portalupi, F. Ciccacci, M. Zacchigna, M. Zangrando, Phys. Rev. B 70 (2004) 235420.
[18] G. Li, C.W. Leung, Y.-J. Wu, A.-C. Sun, J.H. Hsu, P.T. Lai, K.-W. Lin, P.W.T. Pong, Microelectron. Eng. 110 (2013) 250–255.
[19] Z.Q. Jin, J.P. Liu, J. Phys. D, Appl. Phys. 39 (2006) R227.
[20] K.W. Lin, J.Y. Guo, C.Y. Liu, H. Ouyang, J. van Lierop, N.N. Phuoc, T. Suzuki, Phys. Status Solidi A, Appl. Res. 204 (2007) 3991–3994.
[21] J.P. Liu, C.P. Luo, Y. Liu, D.J. Sellmyer, Appl. Phys. Lett. 72 (1998) 483–485.
[22] D.C. Jiles, Acta Mater. 51 (2003) 5907–5939.
[23] J.-Y. Guo, J.v. Lierop, S.-Y. Chang, K.-W. Lin, Jpn. J. Appl. Phys. 48 (2009) 073004.
[24] J.X. Shen, M.T. Kief, J. Appl. Phys. 79 (1996) 5008–5010.
[25] C. Yan, J. Yu, W.-L. Zhou, J.-F. Xie, J.-X. Gao, D.-X. Zhou, Mater. Sci. Eng. B, Solid-State Mater. Adv. Technol. 99 (2003) 421–424.
[26] L. Thomas, B. Negulescu, Y. Dumont, M. Tessier, N. Keller, A. Wack, M. Guyot, J. Appl. Phys. 93 (2003) 6838–6840.
[27] C.-H. Lai, T.C. Anthony, E. Iwamura, R.L. White, IEEE Trans. Magn. 32 (1996) 3419–3421.
[28] K.W. Lin, M. Mirza, C. Shueh, H.R. Huang, H.F. Hsu, J. van Lierop, Appl. Phys. Lett. 100 (2012) 122409.
[29] H.R. Kaufman, R.S. Robinson, R.I. Seddon, J. Vac. Sci. Technol. A 5 (1987) 2081–2084.
[30] A.K. Pant, S.P. Murarka, C. Shepard, W. Lanford, J. Appl. Phys. 72 (1992) 1833–1836.
[31] X. Li, K.W. Lin, H.T. Liang, P.L. Liu, W.C. Lo, D.L. Cortie, F. Klose, J. van Lierop, L. Li, P.W.T. Pong, Microelectron. Eng. 152 (2016) 41–47.
[32] K. Lin, P. Ko, C. Liu, Z. Guo, J.V. Lierop, in: IEEE Int. Magn. Conf., 2006, p. 950.
[33] T. Watanabe, Y. Suzuki, S. Tanii, H. Oikawa, Philos. Mag. Lett. 62 (1990) 9–17.
[34] D.S. Li, H. Garmestani, S.-s. Yan, M. Elkawni, M.B. Bacaltchuk, H.J. Schneider-Muntau, J.P. Liu, S. Saha, J.A. Barnard, J. Magn. Magn. Mater. 281 (2004) 272–275.
[35] I. Ohnuma, H. Enoki, O. Ikeda, R. Kainuma, H. Ohtani, B. Sundman, K. Ishida, Acta Mater. 50 (2002) 379–393.
[36] S. Uhlenbrock, C. Scharfschwerdt, M. Neumann, G. Illing, H.-J. Freund, J. Phys. Condens. Matter 4 (1992) 7973.
[37] A.P. Grosvenor, M.C. Biesinger, R.S.C. Smart, N.S. McIntyre, Surf. Sci. 600 (2006) 1771–1779.
[38] J. Wang, S. Mao, Z. Liu, Z. Wei, H. Wang, Y. Chen, Y. Wang, ACS Appl. Mater. Interfaces 9 (2017) 7139–7147.
[39] A. Brambilla, A. Picone, D. Giannotti, M. Riva, G. Bussetti, G. Berti, A. Calloni, M. Finazzi, F. Ciccacci, L. Duò, Appl. Surf. Sci. 362 (2016) 374–379.
[40] S. Wang, B. Zhang, C. Zhao, S. Li, M. Zhang, L. Yan, Appl. Surf. Sci. 257 (2011) 3358–3362.
[41] T. Yamashita, P. Hayes, Appl. Surf. Sci. 254 (2008) 2441–2449.
[42] L. Yin, I. Adler, T. Tsang, L.J. Matienzo, S.O. Grim, Chem. Phys. Lett. 24 (1974) 81–84.
[43] A.P. Grosvenor, B.A. Kobe, M.C. Biesinger, N.S. McIntyre, Surf. Interface Anal. 36 (2004) 1564–1574.
[44] D. Wilson, M.A. Langell, Appl. Surf. Sci. 303 (2014) 6–13.
[45] H. Singh, A.K. Sinha, M.N. Singh, P. Tiwari, D.M. Phase, S.K. Deb, J. Phys. Chem. Solids 75 (2014) 397–402.
[46] W.A. Brainard, D.R. Wheeler, J. Vac. Sci. Technol. 15 (1978) 1800–1805.
[47] A.M. Venezia, R. Bertoncello, G. Deganello, Surf. Interface Anal. 23 (1995) 239–247.
[48] H.S. O'Neill, Am. Mineral. 72 (1987) 280–291.
[49] M.E. Huntelaar, E.H.P. Cordfunke, W. Ouweltjes, J. Chem. Thermodyn. 24 (1992) 139–143.
[50] D.R. Lide, CRC Handbook of Chemistry and Physics, CRC Press, 2004.
[51] T. Akira, I. Akihisa, Mater. Trans., JIM 41 (2000) 1372–1378.
[52] J.W. Freeland, D.J. Keavney, R. Winarski, P. Ryan, J.M. Slaughter, R.W. Dave, J. Janesky, Phys. Rev. B 67 (2003) 134411.
[53] T. Uemura, T. Marukame, K.i. Matsuda, M. Yamamoto, IEEE Trans. Magn. 43 (2007) 2791–2793.
[54] T. Kuschel, J. Hamrle, J. Pištora, K. Saito, S. Bosu, Y. Sakuraba, K. Takanashi, J. Wollschläger, J. Phys. D, Appl. Phys. 45 (2012) 495002.
[55] P.R. Ohodnicki, J. Long, D.E. Laughlin, M.E. McHenry, V. Keylin, J. Huth, J. Appl. Phys. 104 (2008) 113909.

[56] J.G. Wan, X.W. Wang, Y.J. Wu, M. Zeng, Y. Wang, H. Jiang, W.Q. Zhou, G.H. Wang, J.-M. Liu, Appl. Phys. Lett. 86 (2005) 122501.
[57] I.O. Dzhun, S.A. Dushenko, N.G. Chechenin, E.A. Konstantinova, J. Phys. Conf. Ser. 303 (2011) 012103.
[58] X. Li, K.W. Lin, W.C. Yeh, R.D. Desautels, J. van Lierop, P.W.T. Pong, Phys. Lett. A 381 (2017) 524–528.
[59] J. van Lierop, B.W. Southern, K.W. Lin, Z.Y. Guo, C.L. Harland, R.A. Rosenberg, J.W. Freeland, Phys. Rev. B 76 (2007) 224432.
[60] J. van Lierop, K.-W. Lin, Z.-Y. Guo, P.-H. Ko, H. Ouyang, J. Appl. Phys. 101 (2007) 09E505.
[61] M.J. Carey, A.E. Berkowitz, Appl. Phys. Lett. 60 (1992) 3060–3062.
[62] J.A. De Toro, D.P. Marques, P. Muñiz, V. Skumryev, J. Sort, D. Givord, J. Nogués, Phys. Rev. Lett. 115 (2015) 057201.
[63] K. Maaz, A. Mumtaz, S.K. Hasanain, M.F. Bertino, J. Magn. Magn. Mater. 322 (2010) 2199–2202.
[64] M.D. Stiles, R.D. McMichael, Phys. Rev. B 60 (1999) 12950–12956.
[65] K. Takano, R.H. Kodama, A.E. Berkowitz, W. Cao, G. Thomas, Phys. Rev. B 79 (1997) 1130.
[66] C.-H. Hsiao, R.D. Desautels, J. van Lierop, K.-W. Lin, C.-C. Chi, S. Wang, T.-L. Lin, H. Ouyang, J. Appl. Phys. 115 (2014) 17D724.